

Aerodynamic characteristics and mechanisms for bionic airfoils with different spacings

Cite as: Phys. Fluids **33**, 064101 (2021); <https://doi.org/10.1063/5.0049704>

Submitted: 08 March 2021 . Accepted: 28 April 2021 . Published Online: 01 June 2021

 Deyou Li (李德友),  Hong Chang (常洪),  Zhigang Zuo (左志钢),  Hongjie Wang (王洪杰), and Shuhong Liu (刘树红)



[View Online](#)



[Export Citation](#)



[CrossMark](#)

ARTICLES YOU MAY BE INTERESTED IN

Fluid-structure interaction of a flexible membrane under movement-induced excitation (MIE), extraneously induced excitation (EIE), and coupled MIE-EIE

Physics of Fluids **33**, 065101 (2021); <https://doi.org/10.1063/5.0051559>

The effect of batoid inspired undulating motions on the propulsive forces of a circular planform

Physics of Fluids **33**, 061901 (2021); <https://doi.org/10.1063/5.0046996>

A high-fidelity numerical study on the propulsive performance of pitching flexible plates

Physics of Fluids **33**, 051901 (2021); <https://doi.org/10.1063/5.0049217>

Physics of Fluids
SPECIAL TOPIC: Tribute to
Frank M. White on his 88th Anniversary

SUBMIT TODAY!

Aerodynamic characteristics and mechanisms for bionic airfoils with different spacings

Cite as: Phys. Fluids 33, 064101 (2021); doi: 10.1063/5.0049704

Submitted: 8 March 2021 · Accepted: 28 April 2021 ·

Published Online: 1 June 2021



View Online



Export Citation



CrossMark

Deyou Li (李德友),^{1,a)} Hong Chang (常洪),^{1,a)} Zhigang Zuo (左志钢),^{2,b)} Hongjie Wang (王洪杰),^{1,b)} and Shuhong Liu (刘树红)^{2,a)}

AFFILIATIONS

¹School of Energy Science and Engineering, Harbin Institute of Technology, Harbin, Heilongjiang 150001, China

²State Key Laboratory of Hydro Science and Engineering, Department of Energy and Power Engineering, Tsinghua University, Beijing 100084, China

^{a)}Electronic addresses: lideyou@hit.edu.cn; changhonghit@163.com; and liushuhong@mail.tsinghua.edu.cn

^{b)}Authors to whom correspondence should be addressed: zhigang200@tsinghua.edu.cn and wanghongjie@hit.edu.cn

ABSTRACT

In this study, the aerodynamic characteristics of multi-protuberance airfoils modeled on the fin of a humpback whale were investigated by numerically simulating the National Advisory Committee for Aeronautics 634-021 airfoils. For a Reynolds number of 1.8×10^5 , the numerical simulation results obtained with no spacing between protuberances were compared with experimental values to verify the accuracy of the numerical method. The effects of different spacings on the aerodynamic performance of the airfoil at various angles of attack were investigated by setting the spacing between the two protuberances as 0.25, 0.5, and 0.75c. The results show that the lift coefficient was increased by 5%–15%, and the drag coefficient remained constant under different conditions when the spacing between the protuberances was 0.25c. The twin-protuberance airfoils with different spacings exhibited similar two-step stall characteristics. However, only the unspaced twin-protuberance airfoil had a one-sided stall. Simulations of the multi-protuberance airfoil showed that airfoils featuring spacings between protuberances exhibited good lift characteristics at large angles of attack. With an increase in the angle of attack, the lift coefficient steadily changed. Compared with the full-protuberance airfoil, the drag coefficient of the airfoil with spacing was significantly reduced.

Published under an exclusive license by AIP Publishing. <https://doi.org/10.1063/5.0049704>

NOMENCLATURE

A	Amplitude of leading-edge protuberance, m
AOA	Angle of attack
b	Spacing between protuberances, m
c	Length of airfoil chord, m
C_L	Lift coefficient
C_D	Drag coefficient
l	Length of wingspan, m
Re	Reynolds number
U	Average velocity of air, m s^{-1}
V_x	x Component of velocity, m s^{-1}
V_y	y Component of velocity, m s^{-1}
V_z	z Component of velocity, m s^{-1}
λ	Wavelength of the leading-edge protuberance, m
μ	Dynamic viscosity, $\text{kg m}^{-1} \text{s}^{-1}$
ρ	Density of air, kg m^{-3}
Ω_x	x -Direction vorticity, s^{-1}

I. INTRODUCTION

Airfoil stall-induced problems occur frequently; hence, numerous methods have been proposed to improve or suppress the stall. These control methods can be classified as active or passive control methods depending on whether externally applied energy is required. Active control methods include synthetic jets^{1,2} and simultaneous blowing-suction.^{3,4} Passive control methods include vortex generators,⁵ wing spoilers, and leading-edge protuberances. Compared with active control methods, passive control offers a simple structure and is inexpensive. Among these methods, the bionic leading-edge protuberance structure obtained by observing the humpback whale has become an area of intense research interest. Inspired by this, numerous researchers have attempted to integrate leading-edge protuberances into various fluid machineries to improve their mechanical properties. Guo *et al.*⁶ reported that a bionic leading-edge guide vane could effectively improve the hump effect of pump turbines by appropriately adjusting the amplitude and wavelength. Lin and Chiu⁷ used an experimental

method to test a wind turbine featuring protuberances blades under different operational conditions and found that the protuberance blades stabilized the output power of the wind turbine and improved its average output power. Several researchers have applied bionic airfoils to reduce noise⁸ and limit cavitation.^{9,10} These results show that the leading-edge protuberance is important to ensure the safety of the unit operation and improve its performance. Therefore, it is necessary to explore the mechanisms and influencing factors of leading-edge protuberance. To derive an improvement mechanism applicable to engineering, initial researchers of bionic leading-edge airfoils have established a simplified model based on the shape of humpback whale flippers to perform experimental or numerical simulation analyses. In 1995, Fish and Battle¹¹ mapped the shape of humpback whale flippers and studied their unique leading-edge protuberances, finding that they had a notable effect on the lift coefficient. Miklosovic *et al.*¹² conducted wind tunnel experiments on airfoils with cross-sectional changes and found that the bionic leading edge increased the stall angle of attack (AOA) by approximately 40% and the maximum lift coefficient by 6%. Subsequently, numerous researchers have verified the lift and drag reduction performance of bionic leading edges via numerical simulations and experiments.^{13–17}

Investigations on the mechanism of the leading-edge protuberance are difficult because the chord length of the flipper is constantly changing. To further deepen the analysis of the flow field around the leading-edge protuberance airfoil, a basic airfoil whose chord length remains unchanged has been widely adopted as the modification basis. In terms of aerodynamic characteristics improvement, Rostamzadeh *et al.*^{18,19} and Wang²⁰ reported that the bionic leading-edge airfoil featured smoother stall characteristics. After the stall, the lift coefficient increased by 18%, lift-drag ratio increased by 12%, and the drag coefficient decreased by 10%.

In recent years, in-depth studies of bionic leading-edge airfoils have been conducted to investigate the influence of protuberance parameters, including the number, amplitude, and wavelength of protuberances.

Johari *et al.*¹⁰ investigated the influence of protuberance parameters, and their experimental force measurement results indicated that the protuberance amplitude had a significant impact, whereas the wavelength had a small impact on the airfoil performance. Arai *et al.*²¹ also conducted an in-depth analysis of the protuberance wavelength and showed that the shorter the protuberance wavelength, the higher the lift force of the National Advisory Committee for Aeronautics (NACA) 0018 airfoil at the same post-stall AOA. Favier *et al.*²² conducted parameterized studies on the wavelength and amplitude of the protuberance; when the wavelength was close to c and the amplitude reached $0.07c$, the topology of the wake significantly changed. However, Hansen *et al.*²³ obtained different conclusions, which showed that reducing the wavelength could improve all aspects of lift performance. Cai *et al.*^{24,25} found that a single leading-edge protuberance airfoil exhibited two-step stall characteristics. The stall characteristics were strongly determined by the number of protuberances. The wavelength and amplitude of the protuberance were also found to affect the airfoil performance. The ratio of the protuberance wavelength to its amplitude was taken as a parameter, and the law determining the stall characteristics of the airfoil was obtained.

In 2018, Shanmukha *et al.*²⁶ presented a novel approach. They noted that the first and fourth protuberances on the leading edge of

the humpback fin were significantly larger than the other protuberances, and they designed bionic airfoils with irregular distributions that could be applied to flow-control devices. In 2020, Kant and Bhattacharyya²⁷ designed a new type of twin-protuberance airfoil. The inter-protuberance spacing of the airfoil limited the flow separation zone at large AOAs.

By summarizing previous studies, we identified that the mechanisms of a single-protuberance airfoil have been extensively studied. Multiple protuberances have been used to provide a more reasonable explanation for the flow field. However, choosing appropriate protuberance parameters and quantities to improve the aerodynamic performance of the airfoil remains a problem that must be solved. Therefore, based on previous studies, this study focuses on the influence of inter-protuberance spacing on the performance of twin leading-edge protuberance airfoils. Through numerical simulation of the flow field, the influence and mechanism of this spacing on airfoil performance were further revealed.

II. COMPUTATIONAL MODEL AND NUMERICAL SCHEMES

A. Computational domain

By comparing the shapes of the leading-edge protuberances employed in previous studies, continuous sinusoidal leading-edge protuberances were found to significantly improve the aerodynamic performance of the airfoil. Therefore, a sinusoidal leading-edge protuberance airfoil was selected for the numerical simulation in this study. The airfoil model is shown in Fig. 1. The excellent predation ability of the humpback whale was related to the protuberance of the leading edge of its fin. NACA 63₄-021 was chosen because it has the highest cross-sectional resemblance to the humpback fin. The base profile of all airfoils used in our calculations was the NACA 63₄-021 airfoil. The equation for the protuberance contour is as follows:

$$y = \frac{A}{2} \cdot \cos\left(\frac{2\pi}{\lambda} \cdot x\right) + \frac{A}{2}. \quad (1)$$

Compared with the base airfoil, the single-protuberance airfoil features a single-protuberance at the center of the leading edge, and the twin-protuberance airfoil has two symmetric protuberances at the center of the leading edge. The parameters of the three-dimensional (3D) airfoil were selected according to Ref. 28. The span length of the airfoil was $l = 0.65$ m, and the chord length of the airfoil section without protuberance was $c = 0.2$ m. The leading-edge protuberance parameters were as follows: protuberance amplitude $A = 0.02$ m and protuberance wavelength $\lambda = 0.05$ m. The spacing between protuberances was used as a reference for the protuberance wavelength, and the spacing was $b_0 = 0$ (B_0), $b_1 = \lambda$ (B_1), $b_2 = 2\lambda$ (B_2), and $b_3 = 3\lambda$ (B_3).

To ensure full flow development during the investigation, the distances between the inlet and outlet of the calculation domain and the trailing edge of the airfoil were set to 15 and 25 c , respectively. The wingspan direction width was equal to the wingspan length of the airfoil. A schematic diagram of the calculation domain is presented in Fig. 2.

B. Grid generation and boundary conditions

The computational domain employed a structured grid and was refined on the airfoil surface. The Richardson extrapolation method was used to verify the independence of the number of nodes to reduce

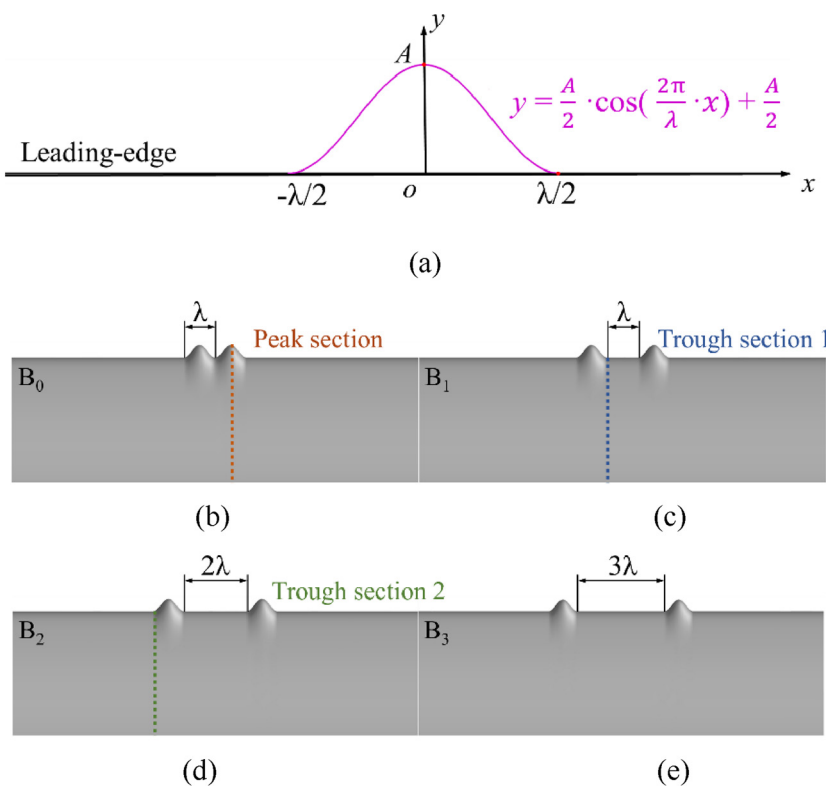


FIG. 1. Airfoil model: (a) leading-edge profile and airfoil model with (b) $b = 0$, (c) $b = \lambda$, (d) $b = 2\lambda$, and (e) $b = 3\lambda$.

the calculation error produced by the number of grid nodes. In Fig. 1 (c), three grids with $N_1 = 11.5 \times 10^6$, $N_2 = 5.19 \times 10^6$, and $N_3 = 2.3 \times 10^6$ nodes were selected for calculation. The airfoil AOA was set to 8° . The lift coefficient was chosen as the grid independence test reference quantity $\Phi = C_L$, where

$$C_L = \frac{L}{0.5\rho U^2 cl}. \quad (2)$$

The values of each variable were determined from the relationships between the parameters,²⁹ as shown in Table I. The ratio between the side lengths of the two sets of grid cells exceeded 1.3, which satisfied the requirements. The extrapolation value was $\Phi_{ext}^{21} = 0.82934$, the approximate relative error was $e_a^{21} = 1.131\%$, the extrapolated relative error was $e_{ext}^{21} = 0.315\%$, and the fine-grid convergence index was $GCI_{fine}^{21} = 0.395\%$. Therefore, $N_1 = 11.5 \times 10^6$ represents a reliable choice for calculation. The C-type partition method was adopted over the entire computational domain. Subsequently, the mesh around the airfoil was refined. The mesh height of the first layer was set to 1×10^{-5} m, and the grid growth ratio

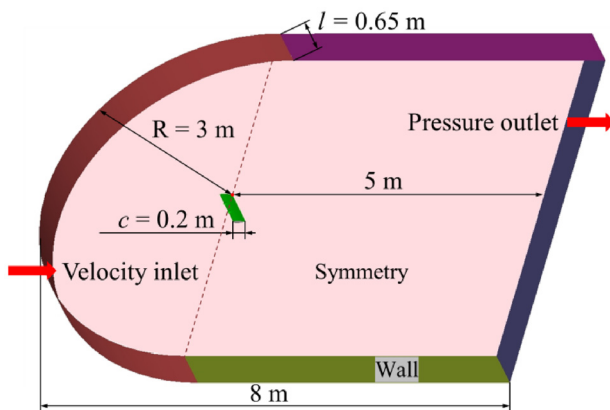


FIG. 2. Computational domain.

TABLE I. Variables employed in the Richardson extrapolation method.

Variable	Value
N_1, N_2, N_3	$11.5, 5.19, 2.3 (\times 10^6)$
r_{21}	1.30369
r_{32}	1.31163
Φ_1, Φ_2, Φ_3	0.8267, 0.8174, 0.8152
p	5.7355
Φ_{ext}^{21}	0.8293
e_a^{21}	1.131%
e_{ext}^{21}	0.315%
GCI_{fine}^{21}	0.395%

was set to 1.1. The computational domain and boundary layer grids are illustrated in Fig. 3.

The Reynolds number was set to 1.8×10^5 for calculation. The flow velocity $U = 13.1$ m/s at the inlet of the calculation domain was calculated via the relationship between the Reynolds number and velocity, expressed as

$$\text{Re} = \frac{\rho c U}{\mu}. \quad (3)$$

Based on the experimental conditions, the turbulence intensity at the inlet was set to 0.2%. The boundary condition of the computational domain outlet was set as the pressure outlet, and the pressure was 101 kPa. The flow on either side of the wingspan had little influence on the flow near the protuberance, and the spanwise flow could be neglected. Therefore, these flows were set as the symmetric boundary conditions. The upper and lower boundaries were far from the airfoil surface; hence, they were set as the wall boundary conditions.

C. Turbulence model selection and numerical schemes

In this study, the air was used as the working medium. The transition shear stress transport (SST), which is suitable for solving the flow field around the airfoil,^{30,31} was adopted to address this problem. The transition SST model uses the momentum thickness Reynolds number as the bridge and introduces two new transport equations based on the SST $k-\omega$ model: the intermittence (turbulent and laminar

flow conversion) and transition initiation criterion. Thus, this model represents a hybrid of transition and SST models. Considering this transition, the SST $k-\omega$ model was adopted. The model equations^{32,33} are expressed as follows.

For the standard $k-\omega$ model, the turbulence kinetic energy, k , and the specific dissipation rate, ω , were obtained from the following transport equations:

$$\frac{\partial(\rho k)}{\partial t} + \frac{\partial(\rho u_i k)}{\partial x_i} = \frac{\partial}{\partial x_j} \left(\Gamma_k \frac{\partial k}{\partial x_j} \right) + G_k^* - Y_k^*, \quad (4)$$

$$\frac{\partial(\rho \omega)}{\partial t} + \frac{\partial(\rho u_i \omega)}{\partial x_i} = \frac{\partial}{\partial x_j} \left(\Gamma_\omega \frac{\partial \omega}{\partial x_j} \right) + G_\omega - Y_\omega + D_\omega. \quad (5)$$

In these equations, G_k represents the generation of turbulence kinetic energy due to mean velocity gradients. G_ω represents the generation of ω . Γ_k and Γ_ω represent the effective diffusivities of k and ω , respectively. Y_k and Y_ω represent the dissipation of k and ω due to turbulence, respectively.

For the transition SST model, the transport equation for the intermittency γ is defined as

$$\frac{\partial(\rho \gamma)}{\partial t} + \frac{\partial(\rho u_j \gamma)}{\partial x_j} = P_{\gamma 1} - E_{\gamma 1} + P_{\gamma 2} - E_{\gamma 2} + \frac{\partial}{\partial x_j} \left[\left(\mu + \frac{\mu_t}{\sigma_y} \right) \frac{\partial \gamma}{\partial x_j} \right]. \quad (6)$$

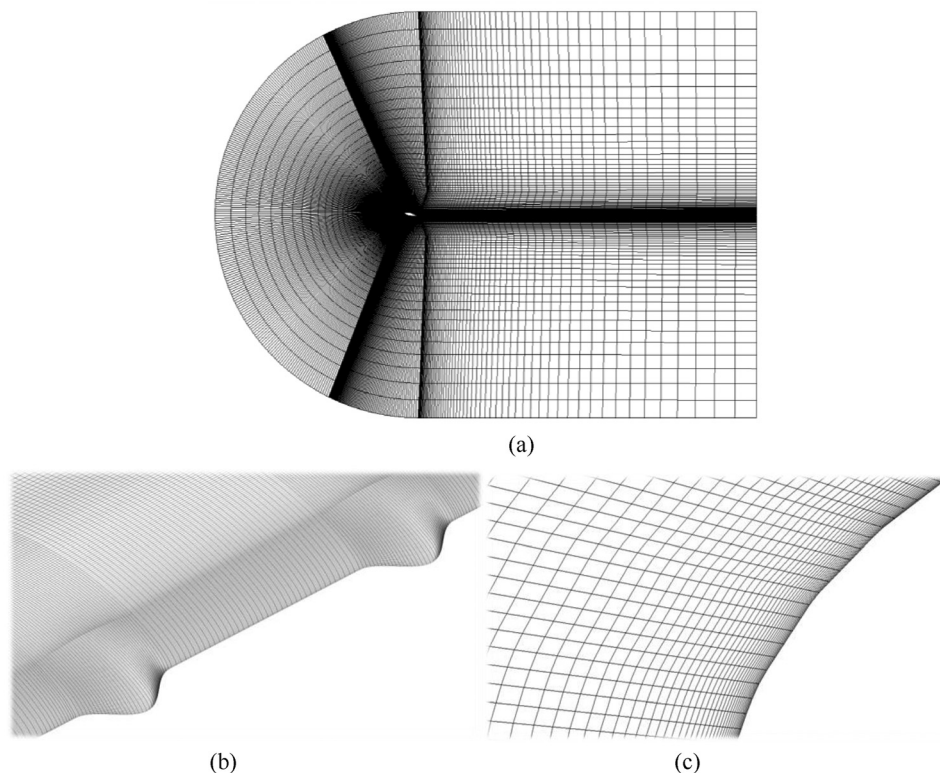


FIG. 3. 3D computational domain grid, (a) C-grid, (b) upper surface grid, and (c) boundary-layer.

The transition sources are defined as follows:

$$P_{\gamma 1} = C_{a1} F_{length} \rho S [\gamma F_{onset}]^{C_{\gamma 3}}, \quad (7)$$

$$E_{\gamma 1} = C_{e1} P_{\gamma 1} \gamma, \quad (8)$$

where S is the strain rate magnitude, F_{length} is an empirical correlation that controls the length of the transition region, and C_{a1} and C_{e1} have values of 2 and 1, respectively. The destruction/relaminarization sources are defined as follows:

$$P_{\gamma 2} = C_{a2} \rho \Omega \gamma F_{turb}, \quad (9)$$

$$E_{\gamma 2} = C_{e2} P_{\gamma 2} \gamma, \quad (10)$$

where Ω is the vorticity magnitude. The transition onset was controlled by the following functions:

$$Re_V = \frac{\rho y^2 S}{\mu}, \quad (11)$$

$$R_T = \frac{\rho k}{\mu \omega}, \quad (12)$$

$$F_{onset1} = \frac{Re_V}{2193 Re_{\theta c}}, \quad (13)$$

$$F_{onset2} = \min(\max(F_{onset1}, F_{onset1}^4), 2.0), \quad (14)$$

$$F_{onset3} = \max\left(1 - \left(\frac{R_T}{25}\right)^3, 0\right), \quad (15)$$

$$F_{onset} = \max(F_{onset2} - F_{onset3}, 0), \quad (16)$$

$$F_{turb} = e^{-\left(\frac{R_T}{4}\right)^4}, \quad (17)$$

where y is the wall distance and $Re_{\theta c}$ is the critical Reynolds number at which the intermittency first starts to increase in the boundary layer. This occurs upstream of the transition Reynolds number $R\tilde{\theta}_t$, and the difference between the two must be obtained from an empirical correlation. Both F_{length} and $Re_{\theta c}$ correlations are functions of $R\tilde{\theta}_t$.

The constants for the intermittency equation are as follows:

$$C_{a1} = 2; \quad C_{e1} = 1; \quad C_{a2} = 0.06; \quad C_{e2} = 50; \quad C_{\gamma 3} = 0.5; \quad \sigma_{\gamma} = 1. \quad (18)$$

The transport equation for the transition momentum thickness Reynolds number $R\tilde{\theta}_t$ is

$$\frac{\partial(\rho R\tilde{\theta}_t)}{\partial t} + \frac{\partial(\rho u_j R\tilde{\theta}_t)}{\partial x_j} = P_{\theta t} + \frac{\partial}{\partial x_j} \left[\sigma_{\theta t} (\mu + \mu_t) \frac{\partial R\tilde{\theta}_t}{\partial x_j} \right]. \quad (19)$$

The source terms are defined as follows:

$$P_{\theta t} = c_{\theta t} \frac{\rho}{t} (Re_{\theta t} - R\tilde{\theta}_t) (1 - F_{\theta t}), \quad (20)$$

$$t = \frac{500 \mu}{\rho U^2}, \quad (21)$$

$$F_{\theta t} = \min \left(\max \left(F_{wake} e^{-\left(\frac{y}{\theta}\right)}, 1.0 - \left(\frac{\gamma - 1/50}{1.0 - 1/50} \right)^2 \right), 1.0 \right), \quad (22)$$

$$\theta_{\theta L} = \frac{R\tilde{\theta}_t \mu}{\rho U}, \quad (23)$$

$$\delta_{BL} = \frac{15}{2} \theta_{BL}, \quad (24)$$

$$\delta = \frac{50 \Omega y}{U} \delta_{BL}, \quad (25)$$

$$Re_{\omega} = \frac{\rho \omega y^2}{\mu}, \quad (26)$$

$$F_{wake} = e^{-\left(\frac{Re_{\omega}}{1E+5}\right)^2}. \quad (27)$$

The model constants for the $R\tilde{\theta}_t$ equation are as follows:

$$C_{\theta t} = 0.03; \quad \sigma_{\theta t} = 2.0. \quad (28)$$

Equations (4)–(6) and (19) constitute the basic equations of the transition SST model.

The governing equations of the fluid are nonlinear partial differential equations that are difficult to solve directly. The finite volume method was used to discretize the pressure and velocity. Then, the SIMPLEC algorithm was applied to solve it. When establishing discrete equations, it is necessary to choose an appropriate discretization scheme for each term in the equation. In this study, a second-order upwind scheme was used to discretize the governing equation terms. The time step was 0.002 s, and each step was iterated 40 times. The convergence criterion was determined to be a calculation residual of less than 10^{-4} .

III. RESULTS AND DISCUSSION

A. Influence of inter-protuberance spacing on the flow

To ensure the accuracy of the numerical simulation, the performance characteristics obtained from numerical simulations of the twin-protuberance airfoil were first compared with their experimental values,³⁴ as shown in Fig. 4. The numerical simulation was conducted for only ten conditions using a positive AOA for each airfoil. Based on the performance characteristics, the AOA (from 0° to 30°) was divided into three regions. The AOA increased through the pre-stall region (A), first-stall region (B), and deep-stall region (C). Figure 4(a) shows the variation in the lift coefficient with respect to AOA. The overall tendency of the numerical simulation values was found to be consistent with the experimental values. The deviation was larger only at the junctions between different regions. As shown in Fig. 4(b), the drag coefficient obtained by the numerical simulation was less than the experimental value. By analyzing the composition of the airfoil drag, the main source of error was the friction drag, and the deviation of the pressure drag was not large. In the calculation, the roughness height of the airfoil surface was 0 m, and the roughness constant was 0.5. The roughness of the experimental model could not be reasonably estimated, which led to a small drag coefficient in the calculation results. The tendency of the drag coefficient was essentially consistent, and the drag coefficient obtained via numerical simulation was relatively small for large AOAs. We concluded that the numerical simulation method was reliable. Therefore, the numerical simulation results of the operational conditions with and without spacing between the protuberances are compared below.

To investigate the reasons for the change in the lift–drag characteristics, the iso-surface of $V_x = 0$ for B_0 is drawn in Fig. 5. The morphology of the separation zone on the upper surface of the airfoil was analyzed according to the three regions marked in Fig. 4. As shown in Fig. 5, under an increase in AOA, the distribution rule for several

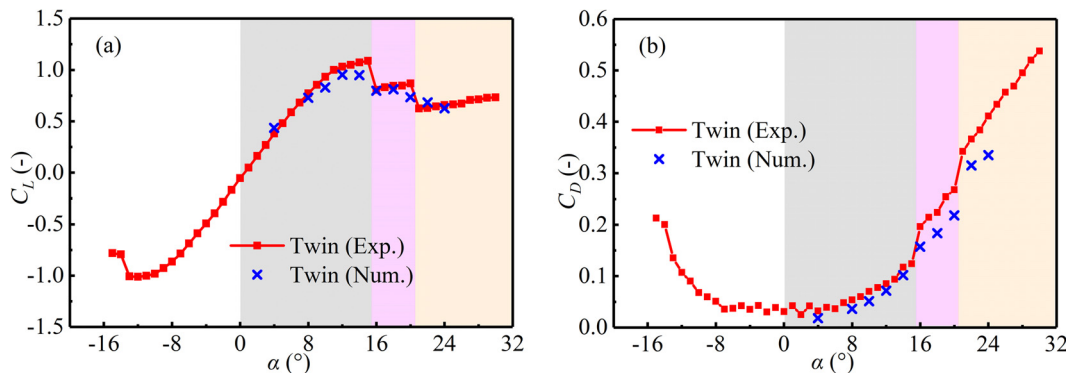


FIG. 4. Comparison of the experimental³⁴ and numerical simulation values for (a) lift coefficient and (b) drag coefficient of the twin-protuberance airfoil.

operational conditions in region A was such that four zones were formed in the wingspan section from the leading to the trailing edge. These four regions were the laminar attached zone, laminar separation bubble zone, turbulent reattachment zone, and turbulent separation zone. At small AOAs, a separation zone was formed near the leading edge of the middle section of the twin-protuberance, indicating that the interaction of the two protuberances made the section between enter the flow separation state in advance. By comparing the critical operational conditions of regions A and B in Fig. 4, the main difference was that the separation zone near the leading edge was in contact with that developed at the trailing edge, significantly altering the lift-drag characteristics of the airfoil. When the airfoil was in region B, the flow was deflected behind the protuberance. A one-sided stall appeared on the airfoil. As shown in Fig. 5, when the flow at the back of the protuberance turned to the left, a large area of attached flow remained near the leading edge on the left-hand side of the protuberance. In contrast, on the right-hand side of the protuberance, the separation zone extending from the leading to the trailing edges gradually expanded toward the wingtip. When the AOA was in region C, almost the entire airfoil surface entered a state of large separation flow, the only exception being the attachment flow converged by two

protuberances peak sections at the back of the protuberances, where the separation zone of the airfoil surface reverted to a symmetrical distribution.

According to Ref. 25, the wavelength-to-amplitude ratio of a single-protuberance airfoil affects its stall characteristics. Therefore, the protuberance wavelength λ was used as the reference value for the inter-protuberance spacing in this study. Numerical simulations were conducted for the following spacings: $b = \lambda$, $b = 2\lambda$, and $b = 3\lambda$. The lift coefficient and percentage change (with respect to condition B_0) for the same AOA were calculated, as summarized in Table II. The drag coefficient and percentage change (with respect to condition B_0) for identical AOAs are summarized in Table III.

Table III compares the lift coefficients for the same AOA. At an AOA of 8° , the lift coefficient of each operation condition increased by approximately 14% compared to that of the no-spacing condition. At an AOA of 12° , the lift coefficient in the B_1 condition increased by $\sim 10\%$. For B_2 and B_3 , the lift coefficient increased by $\sim 6.5\%$. When the protuberance spacing exceeded 2λ , the increase in the lift coefficient was reduced. At an AOA of 16° , a significant difference was observed: under the B_1 condition, the lift coefficient increased, and under B_2 and B_3 , it decreased by different amounts. At AOAs of 20° and 24° , B_1 was the optimal lift coefficient increment condition. The lift coefficients of B_2 and B_3 decreased with increasing distance.

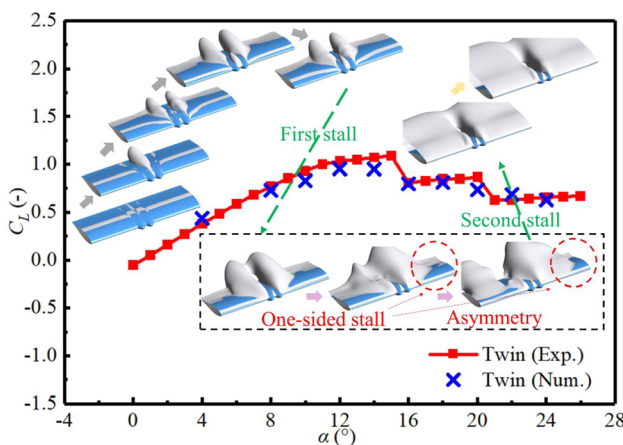


FIG. 5. Iso-surface of $V_x = 0$ for the twin-protuberance airfoil.

TABLE II. Lift coefficient of each condition and changes with respect to $b = 0$.

	$b = 0$	$b = \lambda$	$b = 2\lambda$	$b = 3\lambda$
8°	0.729 37	0.826 73	0.832 52	0.832 45
	0	13.35%	14.14%	14.13%
12°	0.952 66	1.054 41	1.014 69	1.016 48
	0	10.68%	6.51%	6.70%
16°	0.797 99	0.842 31	0.727 39	0.710 45
	0	5.55%	-8.85%	-10.97%
20°	0.734 66	0.864 26	0.852 92	0.842 51
	0	17.64%	16.10%	14.68%
24°	0.626 52	0.705 48	0.660 41	0.637 82
	0	12.60%	5.41%	1.80%

TABLE III. Drag coefficient of each condition and changes with respect to $b = 0$.

	$b = 0$	$b = \lambda$	$b = 2\lambda$	$b = 3\lambda$
8°	0.036 38	0.024 74	0.024 71	0.024 98
	0	-32.00%	-32.08%	-31.34%
12°	0.071 68	0.055 01	0.063 22	0.064 43
	0	-23.26%	-11.80%	-10.11%
16°	0.157 44	0.140 59	0.162 58	0.162 7
	0	-10.70%	3.26%	3.34%
20°	0.218 25	0.211 23	0.220 36	0.224 61
	0	-3.22%	0.97%	2.91%
24°	0.335 16	0.369 65	0.351 18	0.341 54
	0	10.29%	4.78%	1.90%

In contrast to the lift coefficient, the drag coefficient significantly varied at small AOAs and remained constant at large AOAs. As summarized in **Table III**, at an AOA of 8° , the drag coefficient under each operating condition decreased by $\sim 30\%$. At an AOA of 12° , the lift coefficient in the B_1 condition decreased by approximately 23%. For B_2 and B_3 , the drag coefficient decreased by approximately 10%. This drag reduction effect was not as prominent as that observed for B_1 when the spacing exceeded 2λ . When the AOA exceeded 16° , a significant difference was observed. For B_1 , the drag coefficient decreased, and for B_2 and B_3 conditions, it increased by $\sim 3\%$. The drag coefficient changed only slightly for an AOA of 20° . At an AOA of 24° , the drag coefficient for B_1 increased by approximately 10%. The drag coefficients of B_2 and B_3 also increased, but decreased with increasing spacing.

To clarify our comparison of the changes observed under various operational conditions, the numerical simulation results for the airfoil without inter-protuberance spacing were extended to a continuous curve, as shown in **Fig. 6**. The reference line in the **Fig. 4** indicates the trend of numerical simulation results given by experimental values under B_0 condition, which was of no practical significance. From the overall tendency, the three processes of changing the spacing (while retaining the same airfoil stall) were found to have only a certain influence on the numerical value. In addition, the drag coefficient for B_1 increased at 24° , which indicates a superior aerodynamic performance to that obtained for B_0 . The B_2 and B_3 conditions exhibited similar

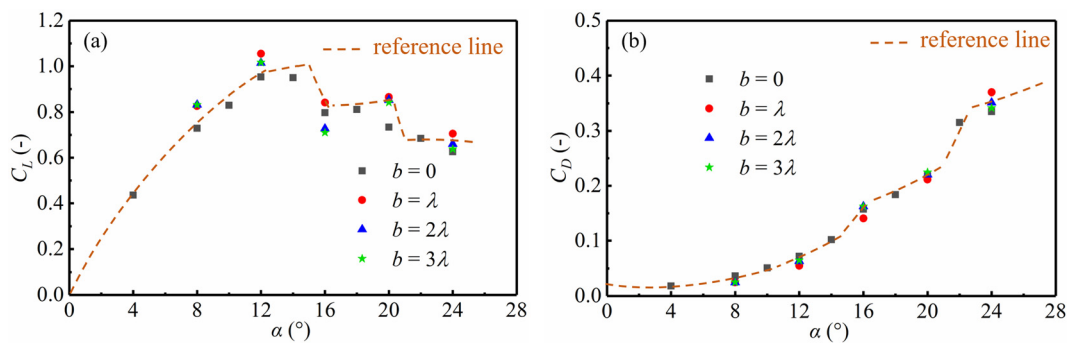
values for each AOA, performed well at small angles, and were essentially identical to the nonspacing airfoil at large angles.

By comparing lift coefficient and drag coefficient, it was found that B_1 airfoil had better aerodynamic characteristics. This phenomenon was further analyzed from the perspective of flow field. The limiting streamlines on the surface 1×10^{-5} m from the upper surface of the airfoil were extracted. Streamwise vortex and iso-surface of $V_x = 0$ are drawn in **Fig. 7**. The vorticity of the x -direction component is expressed as follows:

$$\Omega_x = \frac{1}{2} \left(\frac{\partial v_z}{\partial y} - \frac{\partial v_y}{\partial z} \right). \quad (29)$$

The long and narrow separation bubbles in the middle of the chord for an AOA of 8° are shown in **Fig. 7**. By comparing the flow structures near the airfoil for different inter-protuberance spacings, the operational conditions of B_1 , B_2 , and B_3 were found to be consistent with the distribution form presented. When the AOA was 8° and the distance between the two protuberances was zero, the coupling effect was more prominent, and a concentrated large separation zone was formed. This caused the separation zone to converge behind the protuberances. By comparing the lift coefficients of the four operation conditions (as shown in **Fig. 6**), the conditions for inter-protuberance spacings were found to exhibit superior lift–drag characteristics.

At an AOA of 12° , the flow outside the protuberances remained similar under various conditions, whereas the flow between protuberances showed marked differences. For B_0 , a separation zone was formed in the middle section of the protuberances near the leading edge, and a larger zone was formed downstream. In contrast, when the spacing exceeded λ , long and narrow separation bubbles formed at the leading edge. The separation zone at the trailing edge for B_1 (which exhibited superior performance) was analyzed, and the separation zone was found to have a higher dispersion degree and smaller scale. Similarly, the vortex size was smaller. The distribution of limiting streamlines shows that the front edge of the separation zone behind the protuberances was closer to the trailing edge than that of the other operational conditions. From the analysis of the two conditions distributed in region A, the excellent performance of spaced twin-protuberance airfoils was found to be due to the weakened coupling between protuberances after the spacing was increased. This made the actions of the two protuberances mutually independent, and the flow

**FIG. 6.** Comparison of numerical values for (a) lift and (b) drag coefficients of airfoil under different inter-protuberance spacings.

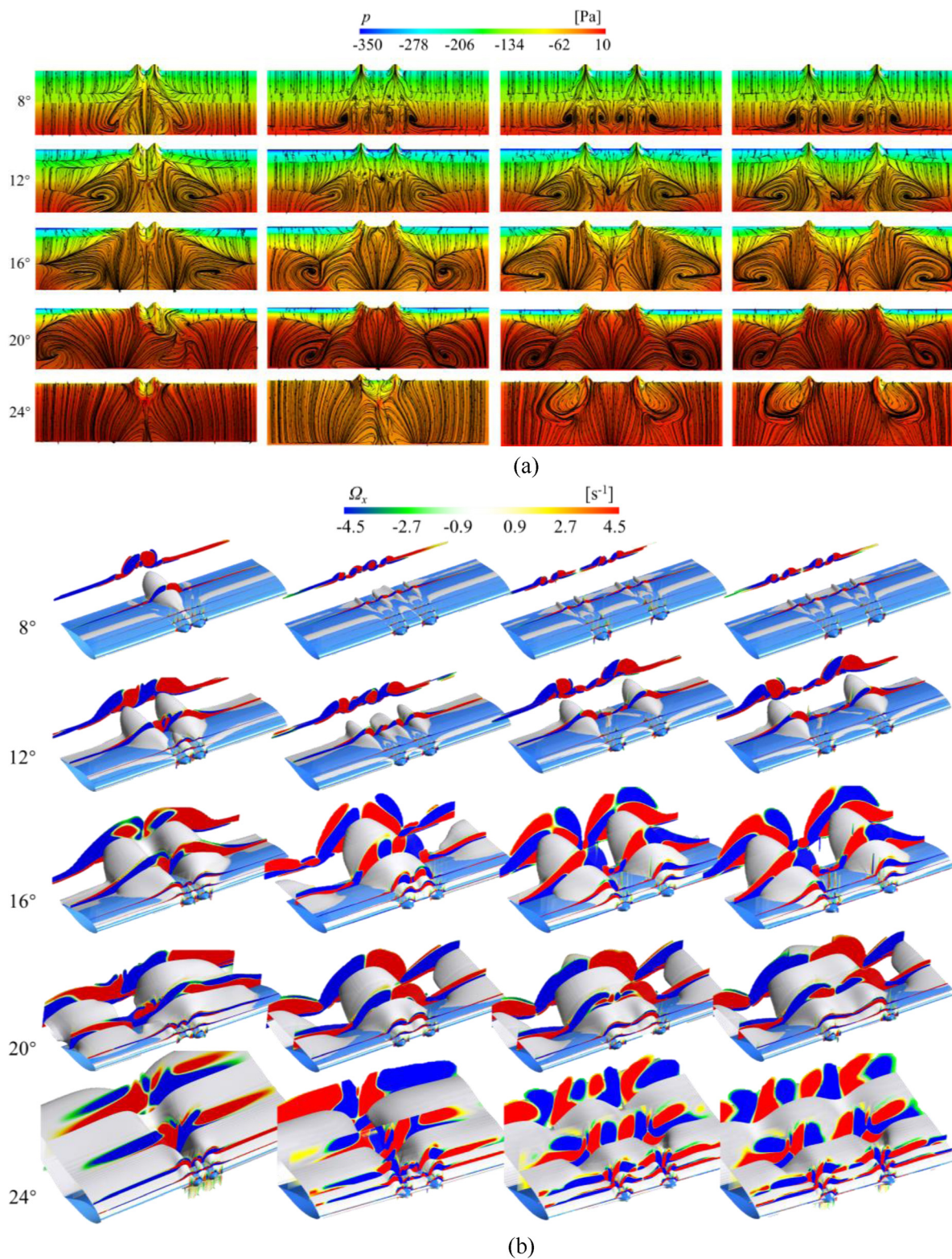


FIG. 7. Flow characteristics of twin-protuberance airfoil, (a) upper-surface limiting streamlines and (b) streamwise vortex and iso-surface of $V_x = 0$.

field resembled that obtained with only one protuberance at the leading edge.

At an AOA of 16° , the airfoil entered the first-stall area, and a separation zone from the leading to the trailing edges appeared in several sections. By comparing the four operational conditions, it was found that B_0 , B_2 , and B_3 exhibited similar flow distribution rules. The middle section between the two-protuberance peak sections was the attachment flow area extending from the leading to the trailing edges, and one part of the attachment flow area near the wingtip was located outside the protuberances. However, for B_1 (which exhibited the optimum performance under this condition), a completely different flow state was observed. The flow separation zone was bound inside by two protuberances, and the flow attachment zone from the leading to trailing edges appeared outside the two protuberances. In pressure analyses of the upper surface of the airfoil, the fluid pressure in the separation zone was found to be higher, and that in the attachment zone was lower. In the B_1 condition, the low-pressure area on the upper-surface leading edge was larger; hence, the airfoil could obtain more lift for this AOA.

At an AOA of 20° , only the airfoil with no spacing between the protuberances exhibited a one-sided stall. By comparing the performance characteristics, we concluded that the one-sided stall was not necessarily related to the two-step stall of the lift–drag characteristics. With an increase in spacing, the area of the attachment flow beyond the protuberances gradually decreased, which corresponded to a decrease in the lift coefficient. Based on the analysis of the two working conditions distributed in region B, the twin-protuberance airfoils with spacing performed well because the protuberances restricted the separation-zone expansion while maintaining flow symmetry.

At an AOA of 24° , the spacing conditions could be classified into two groups according to the flow state. The B_0 and B_1 conditions indicated that two strands of attached flow converged into one strand; in addition, the B_2 and B_3 conditions showed that two strands of attachment flow deviated from each other and turned, respectively. By comparing the flow on the upper surface of different airfoils, it was found that the influence of the leading-edge protuberance on the flow field at different AOAs was the cause of the variation in the distribution of the attached flow and separated flow on the airfoils. The leading-edge protuberance formed the attached flow on the peak section, and the

deflection directly affected the position of the upper surface attached area. This deflected attached flow influenced the separation of the flow field, resulting in the separation zone bound between protuberances or isolated on the outside of protuberances. This effect was similar to that of a single protuberance. Therefore, it is necessary to compare the high-energy fluid generated by single and twin protuberances to determine the reason for the improvement of the aerodynamic characteristics of the leading-edge twin-protuberance airfoil ($\text{twin-}\lambda$). Therefore, we conducted numerical simulations on a single-protuberance airfoil under identical working conditions to determine the influence of spacing on the action range of protuberances.

By analyzing the vorticity distribution for a 24° AOA (as shown in Fig. 8), different vortex structures generated movement tendencies in the fluids near or far from the airfoil. These two tendencies produced flow separation vortex pairs I and II.

B. Influence of spacing on the coupling effect

Several of the above results were verified by numerical simulations of single protuberance airfoils, which are further analyzed in this section. As shown in Fig. 9, compared with the B_0 operational condition, the single-protuberance airfoil achieved a superior lift coefficient and lift–drag ratio. Compared with the single-protuberance airfoil, the lift coefficient and lift–drag ratio were improved for most AOAs under the B_1 condition. The spacing of λ between protuberances was found to be more valuable than a single protuberance.

To clearly observe the flow structure and influence area of the airfoil surface, upper surface V^2 was drawn at a position of 1×10^{-4} m from the upper surface. The V^2 value was calculated by the square of the magnitude of the velocity on the new surface, as shown in Fig. 10. When the AOA was 8° , the flow field behind the protuberance of the single-protuberance airfoil served as the basic flow structure. This structure was reflected in the B_1 , B_2 , and B_3 conditions. In the B_0 condition, the interaction between the two structures reduced the lift coefficient and lift–drag ratio. By comparing the pressure distribution in Fig. 7(a) with the location of the separation zone in Fig. 7(b), it was found that at small AOAs, the formation of concentrated and large-scale areas of separation at the trailing edge reduced the aerodynamic characteristics of the twin-protuberance airfoil. The reason for this

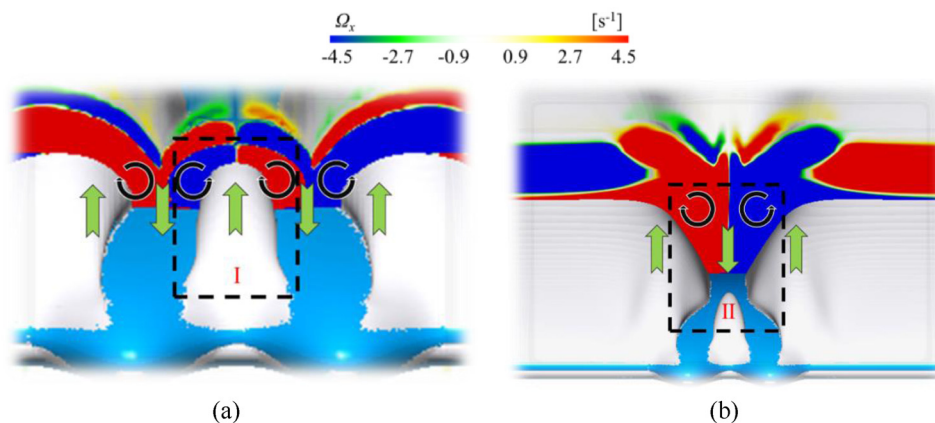


FIG. 8. Relationship between vorticity and separation zone for $\text{AOA} = 24^\circ$: (a) I—separation vortex pair and (b) II—attached vortex pair.

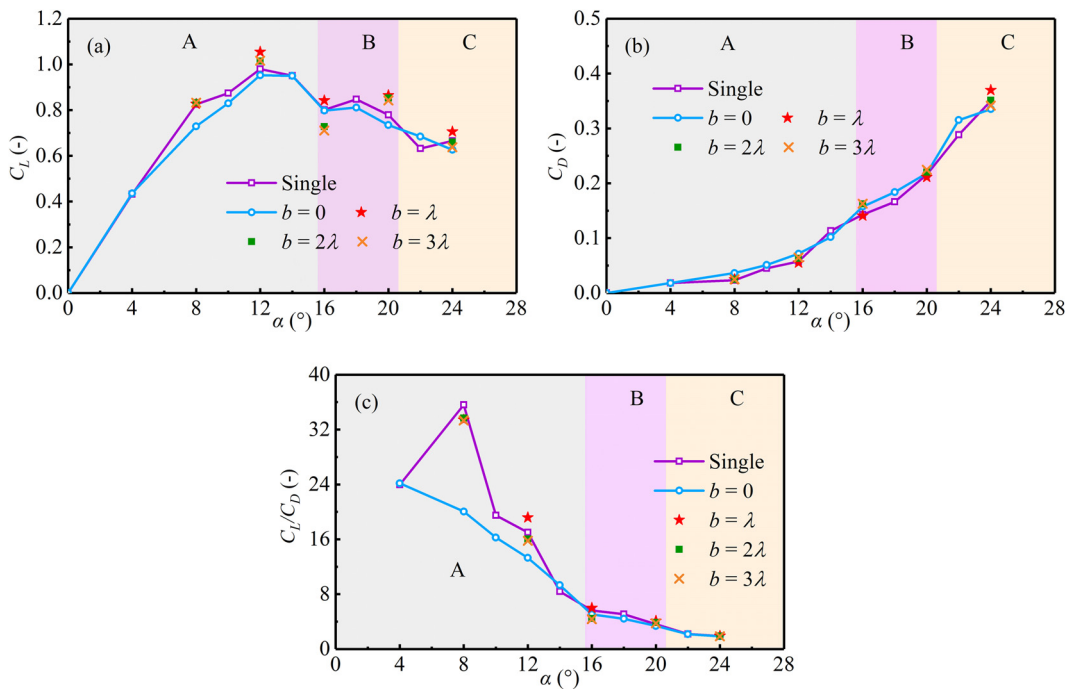


FIG. 9. Numerical comparison of (a) lift coefficients, (b) drag coefficients, and (c) lift–drag ratios of single- and twin-protuberance airfoils.

phenomenon is that the high-pressure area on the upper surface of the airfoil moved to the leading edge owing to the formation of a separate flow at the leading edge of the trough section.

At an AOA of 12° , flow asymmetry was observed at the trailing edge of the single-protuberance airfoil. For B_0 , the coupling effect between the two protuberances retained a sizeable influence on the airfoil. When the spacing was increased to λ , a separation zone appeared between the protuberances, which could be considered as the result of the linear superposition of a single protuberance. When the spacing was increased to 2λ , the kinetic energy distribution could not be obtained as a superposition of a single protuberance. The small deflection near the trailing edge of a single protuberance formed a convergent attached flow region under the combined action of two protuberances. Energy was added to the fluid between the protuberances owing to the deflection of the high-energy fluid. The fluid with higher energy could overcome the adverse pressure gradient of the flow, thereby allowing the fluid between the protuberances to remain attached. In addition, the deflection range of the attachment flow was measured, and the deflection tendency became more prominent as the spacing increased.

According to the analysis of the working conditions in zone B (as shown in Fig. 11), the flow field for B_0 was structurally similar to that of the single-protuberance airfoil. This can explain why the one-sided stall phenomenon resembled that of the single-protuberance airfoil. For other working conditions, the high-energy fluid formed from the leading-edge protuberance exhibited symmetry about the middle section, which could be obtained via linear superposition of the single-protuberance airfoil flow field. The influence range of each protuberance with an expansive shape was 2λ . The influence area of each protuberance with a contracted shape was $\sim 1.5\lambda$.

When the AOA was 24° (as shown in Fig. 12), the influence range of a single protuberance was $\sim 2.5\lambda$. Therefore, the operational conditions B_2 and B_3 were essentially consistent with the lift–drag characteristics of a single-protuberance airfoil. Here, compared with the high-energy fluid distribution for B_1 , the high-energy region was narrower under B_0 ; thus, the attached flow area on the airfoil surface was concentrated in the middle section. However, under condition B_1 , owing to the larger spacing, the attached flow was fully developed, and the attached region and lift coefficient were larger.

By comparing the upper surface V^2 , the findings can be summarized in the following three aspects: with the increase in AOA, the high-energy fluid of the single-protuberance airfoil spontaneously deflected to the wing tip, and the degree of deflection gradually deepened; the action of the leading-edge twin protuberance could be roughly divided into three categories: uncoupling, contraction-type coupling, and dilating-type coupling. The airfoil in the uncoupling state exhibited better aerodynamic performance when it was in the pre-stall area. After the first stall, contraction-type coupling prevailed. At a deep stall, further evaluation is required using different types of impact ranges; under the conditions of small and large AOAs, the flow of airfoils with spacing between the protuberances always tended to be similar to that of airfoils with a single protuberance.

C. Influence of spacing between protuberances on airfoils with full protuberances

We selected continuous leading-edge protuberances as it is not possible to determine protuberance placement in the application process; hence, it was necessary to study the influence of the inter-protuberance spacing in this case. Previous research results

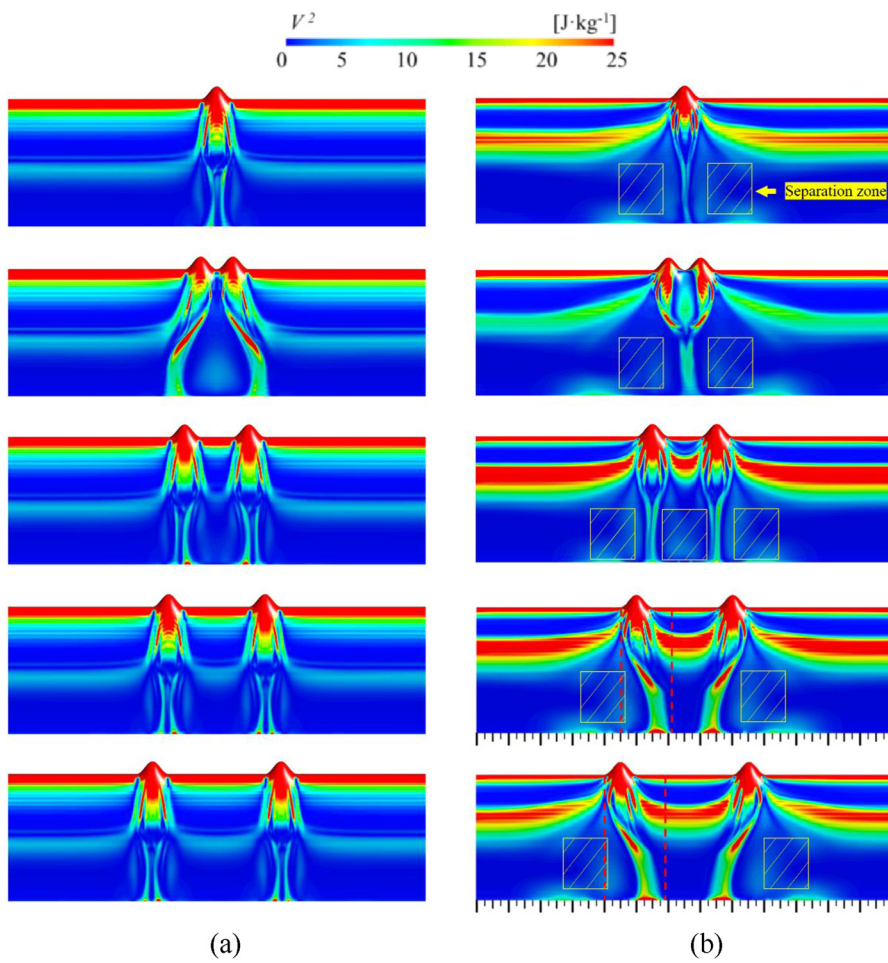


FIG. 10. Upper surface V^2 of region (1) for (a) $\text{AOA} = 8^\circ$ and (b) $\text{AOA} = 12^\circ$.

demonstrate that the twin-protuberance airfoil with B_1 exhibits superior aerodynamic characteristics. Therefore, we compared an airfoil with continuous protuberances with a spacing of λ . The models of the two airfoils are shown in Fig. 13(a). The lift coefficient of the base airfoil linearly increased for small AOAs, and the drag coefficient was below 0.05. When the AOA exceeded 10° , the lift coefficient was maintained near 1, and the drag coefficient was below 0.1. An airfoil stall appeared for AOAs of 18° – 20° , for which the lift coefficient decreased from 1.02 to 0.55 and the drag coefficient increased from 0.11 to 0.24. After the stall, the lift coefficient increased slowly, and the drag coefficient increased rapidly. Compared with the lift coefficient, drag coefficient, and lift–drag ratio of the airfoil at various AOAs, the variation in these values was more useful to study. The variation in the aerodynamic characteristics of each airfoil (with respect to the base airfoil) is shown in Fig. 13. Taking the lift coefficient as an example, the calculation method for each point is as follows:

$$\Delta C_{L(i)} = \frac{C_{L(i)} - C_{L(\text{base})}}{C_{L(\text{base})}}. \quad (30)$$

Figure 13(a) compares the lift coefficient changes of each airfoil, and the lift coefficient increases with respect to the lift coefficient of

the base airfoil only at A, B, and C. The following conclusions can be drawn from the analysis of the lift coefficient.

At small AOAs, airfoils with protuberances exhibited considerably increased lifts. At point A, the lift coefficient of the airfoil with protuberances exceeded that of the base airfoil. When the AOA was increased to 8° , the lift coefficients of the single-protuberance airfoil (single) and the twin-protuberance airfoil with spacing (twin- λ) were slightly higher than those of the base airfoil. The lift coefficient of twin- λ was higher than that of the base airfoil when the AOA was 12° .

Comparing two multi-protuberance airfoils, the spacing between the leading protuberances was found to increase the AOA, and the lift coefficient decreased.

At point C, after exceeding the stall AOA region of the base airfoil, each airfoil exhibited a considerably increased lift once more. The lift coefficient of the twin- λ increased by more than 50%, whereas the others increased by more than 30% for an AOA of 20° . In the deep-stall AOA region, the lift coefficients of the multi-protuberance airfoils (full- λ and full) were more stable, and the increase was maintained at $\sim 30\%$.

Overall, the lift coefficients below the stall AOA were reduced by multi-protuberance (full- λ and full) and increased above the stall

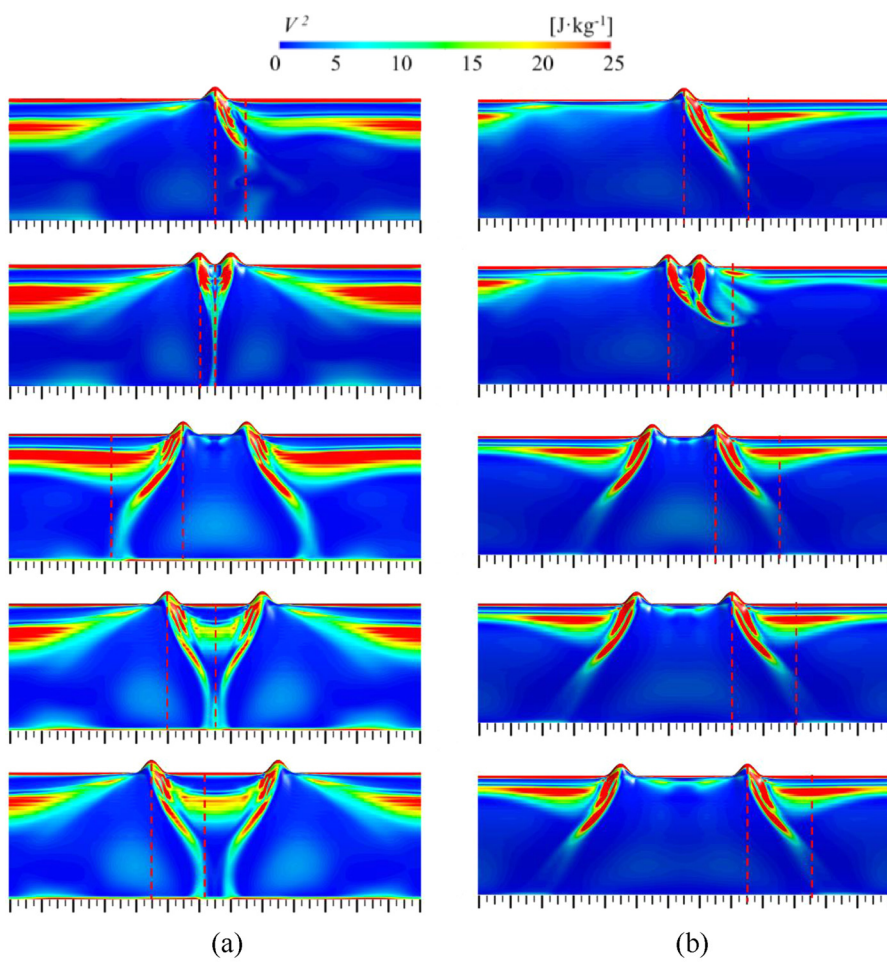


FIG. 11. Upper surface V^2 of region B for (a) $\text{AOA} = 16^\circ$ and (b) $\text{AOA} = 20^\circ$.

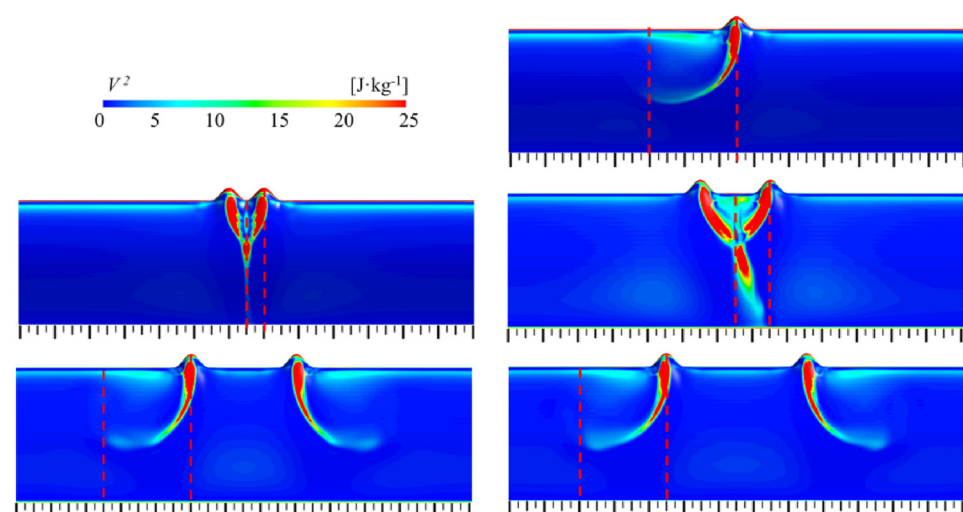


FIG. 12. Upper surface V^2 of region C for $\text{AOA} = 24^\circ$.

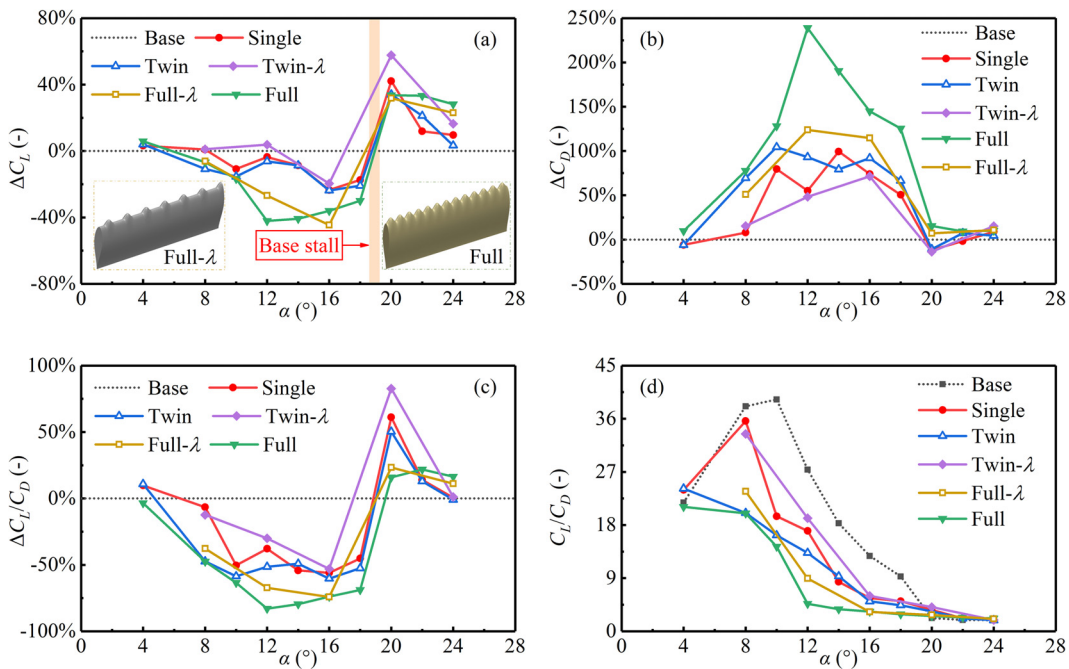


FIG. 13. Numerical comparison of the changes in (a) lift coefficient, (b) drag coefficient, (c) and lift–drag ratio, as well as the (d) lift–drag ratio of the airfoils for different numbers of protuberances.

AOA. As a result, the difference between the lift coefficients before and after the stall decreased. Thus, multi-protuberances increased the stability of the lift coefficient.

In terms of the drag coefficient analysis, as shown in Fig. 13(b), the protuberance generally led to an increase in the drag coefficient for identical AOAs. More significantly, the multi-protuberance airfoil (full) exhibited a significantly increased drag coefficient. However, the multi-protuberance airfoil (full- λ) exhibited drag coefficients similar to those of other airfoils. Two special points are observed below the basic airfoil resistance curve. Both single- and twin-protuberance airfoils showed drag reduction at AOAs of 4° and 20°. In the practical application of airfoils to aircraft-wing design, no special requirements are placed on the drag characteristics of low-speed aircraft. To achieve good maneuverability, there should be maximum increase in the lift coefficient of the aircraft. However, for high-speed aircrafts, the drag characteristics are clear. Excessive aerodynamic force depletes the thrust of the aircraft engine and also promotes stress fatigue of the aircraft body, causing its disintegration. Therefore, the influence of each airfoil on the lift–drag ratio also needs to be explored. As shown in Fig. 13(c), each airfoil increases its lift-to-drag ratio after the stall. Compared with the widely studied multi-protuberance airfoil (full), the lift–drag ratio of the multi-protuberance airfoil (full- λ) was improved to a certain extent. Combined with the variation of the lift and drag coefficients, this phenomenon was observed because the increase in spacing reduced the drag of the airfoil. Furthermore, when the AOA increased to 24°, only the multi-protuberance airfoil (full- λ and full) retained a larger lift–drag ratio than the base airfoil.

V^2 pictures of multi-protuberances airfoil are shown in Fig. 14, and a structure similar to the single and twin-protuberances was

observed at small AOAs. After increasing the AOA, the flow field consistently exhibited flow convergence after the protuberance.

According to the twin-protuberance analysis results, more dispersed flow structures increase the lift coefficient. Compared with the two airfoils for an AOA of 12°, the airfoil flow structure with fewer protuberances was more dispersed; hence, the lift coefficient was higher. At a large AOA, the airfoil with more leading-edge protuberances produced a larger range of high-energy fluids after the protuberances, which effectively allowed the fluid to maintain its attached flow state at large AOAs, thereby maintaining a better lift-acquisition ability at large AOAs. By comparing the relationship between the separation zone and V2 under an AOA of 16° in Fig. 7, it can be seen that the outer part of the contraction-type coupling and the inner part of the dilating-type coupling were flow separation zones. When the AOA was higher than 12°, more small separation zones were formed in the multi-protuberance airfoil, which reduced the flow field interaction between the protuberances. Wall shear was extracted from the upper surface of the airfoil, as shown in Fig. 15, and it was found that when the shear force was relatively large, it was concentrated in the attached flow region formed by the protuberance. At the same time, the integral transformation of wall shear on the lower surface of two types of multi-protuberance airfoils was performed, and the frictional drag values were similar at the same AOA, whereas the integral value of the upper multi-protuberance airfoils (full) was significantly higher than that of the multi-protuberance airfoils (full- λ). This indicated that the increase in the airfoil drag coefficient was a result of the increase in friction caused by the attached flow formed by the protuberance.

The influence of leading-edge protuberances and spacings on airfoil performance could not be fully reflected in the analysis of the

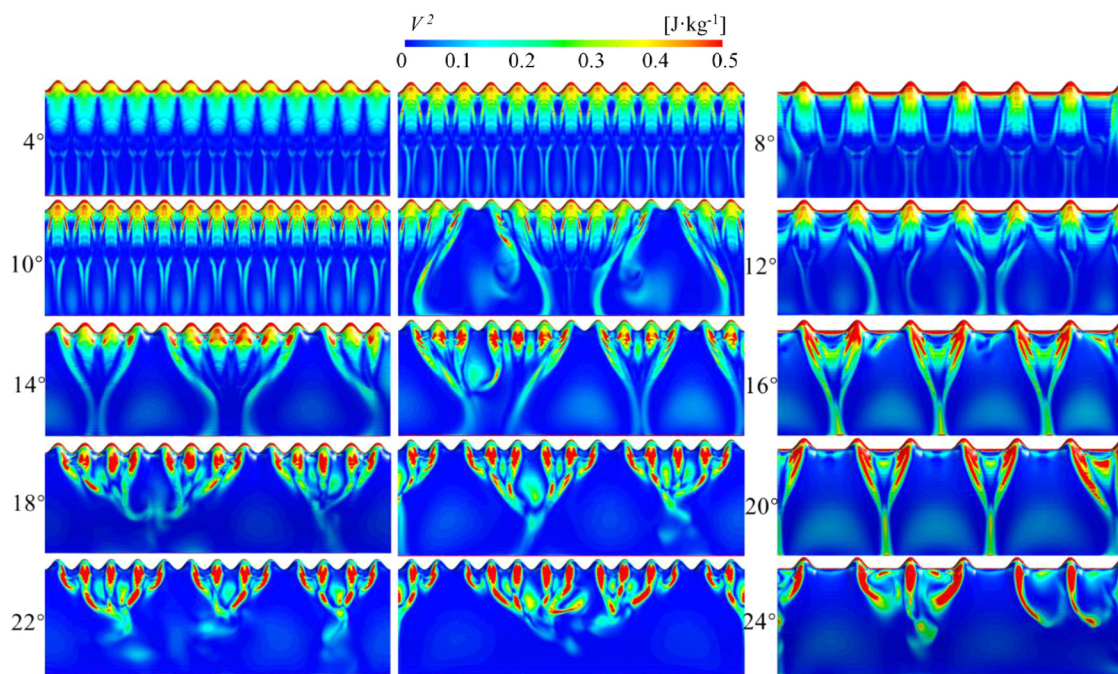


FIG. 14. Upper surface V^2 of airfoils with multiple protuberances.

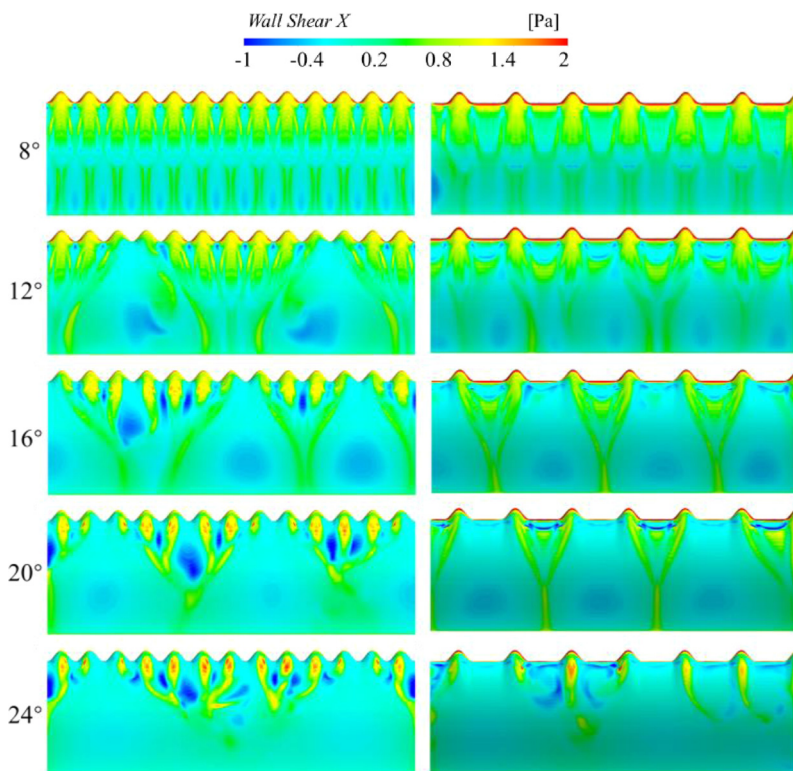


FIG. 15. Upper surface wall shear of airfoils with multiple protuberances.

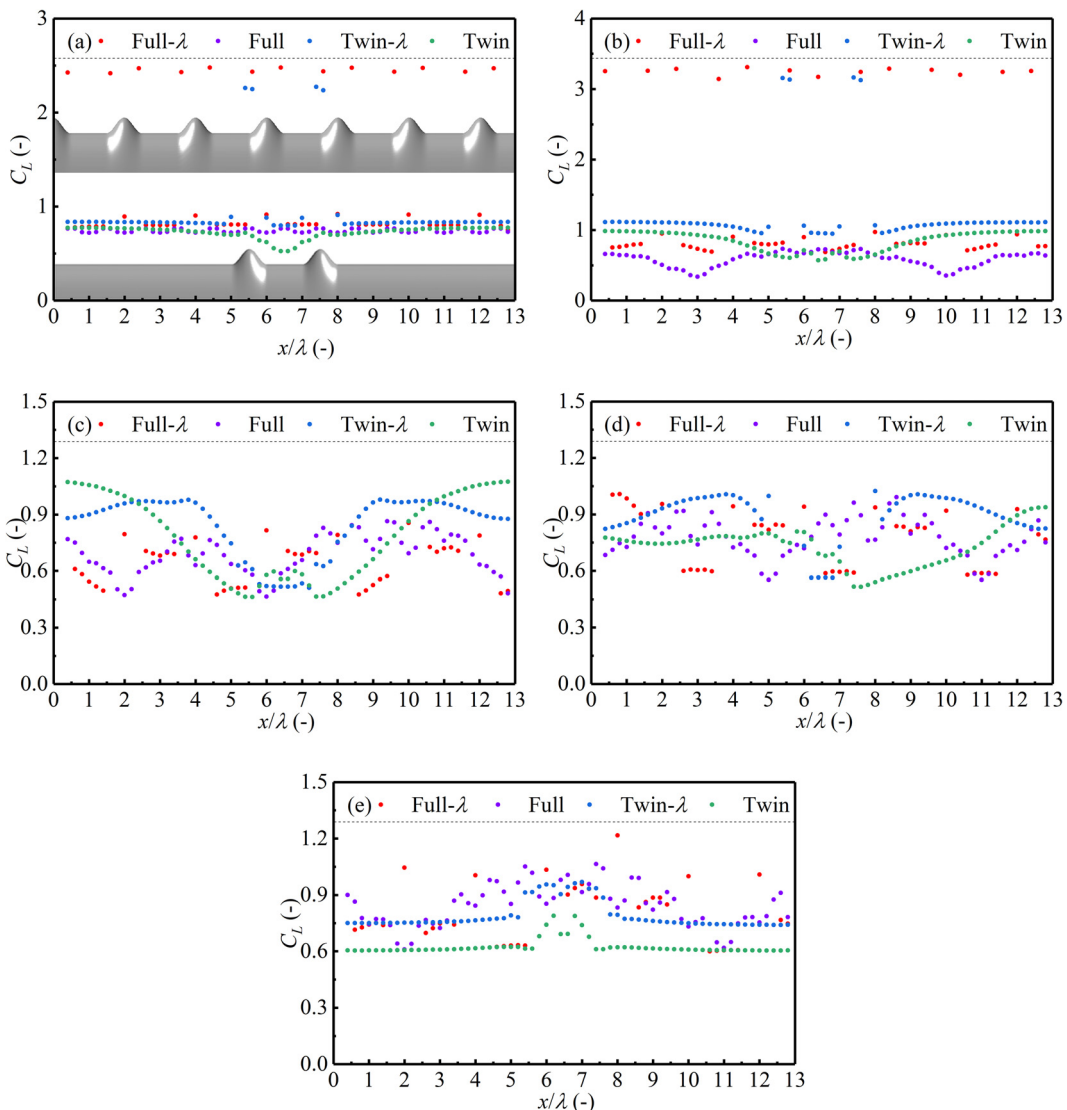


FIG. 16. Section lift coefficient at (a) $\text{AOA} = 8^\circ$, (b) $\text{AOA} = 12^\circ$, (c) $\text{AOA} = 16^\circ$, (d) $\text{AOA} = 20^\circ$, and (e) $\text{AOA} = 24^\circ$.

upper surface only. Therefore, the lift coefficient of the airfoil's section was defined, as shown in Fig. 16, which was the relationship between the section position and the local lift coefficient.

In Fig. 16(a), the leading-edge protuberance significantly improved the local lift coefficient of the peak section of the twin-protuberance airfoil (twin- λ). The lift coefficient of the trough section of the twin-protuberance airfoil (twin) decreased obviously. The same conclusion could be obtained in Fig. 16(b), and it could also be found that for multi-protuberance airfoils, the leading-edge protuberance caused the local lift coefficients of each section to be significantly lower than those for less protuberance airfoils. At $\text{AOA} = 16^\circ$, the lift coefficient of the base airfoil was around 1. By comparing the twin-protuberance airfoil in Fig. 16(c), it was found that the pressure coefficient of the protuberance and adjacent sections decreased as a result of the leading-edge protuberance, leading to a two-step stall

phenomenon of the airfoil. After this AOA, the lift coefficients of most sections of the multi-protuberance airfoil tended to increase, so that the whole lift change process of the airfoil kept a steady growth. After entering the deep stall state, the lift coefficient of most sections of multi-protuberance airfoil was obviously higher than that of others.

IV. CONCLUSIONS

In this study, the effect of different inter-protuberance spacings on a leading-edge twin-protuberance airfoil was studied in detail via numerical simulations. The conclusions are as follows:

- (1) The lift-drag coefficients showed that changing the spacing could effectively improve the stall performance of the twin-protuberance airfoil. In addition, the lifting effect was optimal when the spacing was equal to the protuberance wavelength. The lift coefficient

- increased by more than 10% for small AOAs, ~5% for medium ones, and more than 10% for large AOAs.
- (2) The unsteady numerical simulation results indicated that the unspaced twin-protuberance airfoil section presented a two-step stall phenomenon, accompanied by a one-sided stall phenomenon on the airfoil. This two-step stall phenomenon remained after increasing the spacing between the protuberances. However, in the stall process, the flow field presented an essentially symmetrical distribution, and no one-sided stall phenomenon was observed. No necessary relationship persisted between the one-sided and two-step stall phenomena.
 - (3) The influence of the twin-protuberance airfoil vortexes and separation zones on airfoil performance was analyzed. The higher the dispersion degree of the separation zone, the smaller the scale; similarly, the smaller the streamwise vortex scale, the superior the improvement effect of the airfoil performance characteristics. Based on the analysis of the kinetic energy distribution of the airfoil, the two strands of high-energy fluid for protuberances without spacing were determined to interact with each other. When the spacing was increased, the influence range was similar to that of the single-protuberance airfoil, and the flow field was approximately linearly superimposed.
 - (4) The simulation results for the multi-protuberance airfoil (full- λ and full) showed that multi-protuberance airfoil (full- λ) made the peak point of the reduction of lift coefficient move toward the large AOA. At the same time, the phenomenon of large drag coefficient value of multi-protuberance airfoil (full) was effectively improved by multi-protuberance airfoil (full- λ). Leading-edge protuberances reduced the lift coefficient before stall and increased the drag coefficient, and the lift coefficient after stall increased by approximately 30%.

Through this research it was determined that a protuberance spacing equal to the wavelength condition exhibited substantial applicability. In subsequent studies, this conclusion can be applied to fluid mechanical parts such as turbine guide vanes and wind turbine blades to verify their applicability.

ACKNOWLEDGMENTS

This research was funded by the Natural Science Foundation of Heilongjiang Province (Grant No. LH2020E045) and the Fundamental Research Funds for the Central Universities (Grant No. HIT.NSRIF.2019063) for financial support.

The authors declare no conflict of interest.

DATA AVAILABILITY

The data that support the findings of this study are available from the corresponding authors upon reasonable request.

REFERENCES

- ¹N. Durrani and B. A. Haider, "Study of stall delay over a generic airfoil using synthetic jet actuator," in AIAA Aerospace Sciences Meeting Including the New Horizons Forum and Aerospace Exposition (2015).
- ²C. L. Rumsey, T. B. Gatski, and W. L. Sellers, "Summary of the 2004 CFD validation workshop on synthetic jets and turbulent separation control," in AIAA Flow Control Conference (2004).
- ³M. Genç and Ü. Kaynak, "Control of flow separation and transition point over an aerofoil at low Re number using simultaneous blowing and suction," in 19th AIAA Computational Fluid Dynamics (2009).
- ⁴L. Feng, Z. Li, and Y. Chen, "Lift enhancement strategy and mechanism for a plunging airfoil based on vortex control," *Phys. Fluids* **32**, 087116 (2020).
- ⁵J. B. Huang, Z. X. Xiao, F. U. Song, and M. Zhang, "Study of control effects of vortex generators on a supercritical wing," *Sci. China Technol. Sci.* **53**, 2038–2048 (2010).
- ⁶Z. W. Guo, C. H. Wang, Z. D. Qian, X. W. Luo, and W. P. Xia, "Suppression of hump characteristic for a pump-turbine using leading-edge protuberance," *Proc. Inst. Mech. Eng.* **234**, 187–194 (2020).
- ⁷Y. Lin and P. Chiu, "Influence of leading-edge protuberances of fx63 airfoil for horizontal-axis wind turbine on power performance," *Sustainable Energy Technol. Assess.* **38**, 100675 (2020).
- ⁸M. R. Pendar, E. Esmailifar, and E. Roohi, "LES study of unsteady cavitation characteristics of a 3D hydrofoil with wavy leading edge," *Int. J. Multiphase Flow* **132**, 103415 (2020).
- ⁹Z. H. Li, Z. D. Qian, and B. Ji, "Transient cavitating flow structure and acoustic analysis of a hydrofoil with whalelike wavy leading edge," *Appl. Math. Model.* **85**, 60–88 (2020).
- ¹⁰H. Johari, C. W. Henoch, D. Custodio, and A. Levshin, "Effects of leading-edge protuberances on airfoil performance," *AIAA J.* **45**, 2634–2642 (2007).
- ¹¹F. E. Fish and J. M. Battle, "Hydrodynamic design of the humpback whale flipper," *J. Morphol.* **225**, 51–60 (1995).
- ¹²D. S. Miklosovic, M. M. Murray, L. E. Howle, and F. E. Fish, "Leading-edge tubercles delay stall on humpback whale (*Megaptera novaeangliae*) flippers," *Phys. Fluids* **16**, L39–L42 (2004).
- ¹³H. T. C. Pedro and M. H. Kobayashi, "Numerical study of stall delay on humpback whale flippers," in 46th AIAA Aerospace Sciences Meeting and Exhibit, Reno, NV (2008).
- ¹⁴P. W. Weber, L. E. Howle, M. M. Murray, and D. S. Miklosovic, "Computational evaluation of the performance of lifting surfaces with leading-edge protuberances," *J. Aircr.* **48**, 591–600 (2011).
- ¹⁵D. S. Miklosovic, M. M. Murray, and L. E. Howle, "Experimental evaluation of sinusoidal leading edges," *J. Aircr.* **44**, 1404–1408 (2007).
- ¹⁶E. A. V. Nierop, S. Alben, and M. P. Brenner, "How bumps on whale flippers delay stall: An aerodynamic model," *Phys. Rev. Lett.* **100**, 054502 (2008).
- ¹⁷M. J. Stanway, *Hydrodynamic Effects of Leading-Edge Tubercles on Control Surfaces and in Flapping Foil Propulsion* (Massachusetts Institute of Technology, 2008).
- ¹⁸N. Rostamzadeh, R. M. Kelso, B. B. Dally, and K. L. Hansen, "The effect of undulating leading-edge modifications on NACA 0021 airfoil characteristics," *Phys. Fluids* **25**, 117101 (2013).
- ¹⁹N. Rostamzadeh, K. L. Hansen, R. M. Kelso, and B. B. Dally, "The formation mechanism and impact of streamwise vortices on NACA 0021 airfoil's performance with undulating leading edge modification," *Phys. Fluids* **26**, 107101 (2014).
- ²⁰G. F. Wang, *Study on Flow Separation Control and Application of Bionic Wavy Edge Airfoil* (The University of Chinese Academy of Sciences, 2014).
- ²¹H. Arai, Y. Doi, T. Nakashima, and H. Mutsuda, "A study on stall delay by various wavy leading edges," *J. Aero Aqua Bio-mech.* **1**, 18–23 (2010).
- ²²J. Favier, A. Pinelli, and U. Piomelli, "Control of the separated flow around an airfoil using a wavy leading edge inspired by humpback whale flippers," *C. R. Mec.* **340**, 107–114 (2012).
- ²³K. L. Hansen, R. M. Kelso, and B. B. Dally, "Performance variations of leading-edge tubercles for distinct airfoil profiles," *AIAA J.* **49**, 185–194 (2011).
- ²⁴C. Cai, Z. G. Zuo, M. Morimoto, T. Maeda, Y. Kamada, and S. H. Liu, "Two-step stall characteristic of an airfoil with a single leading-edge protuberance," *AIAA J.* **56**, 64–77 (2018).
- ²⁵C. Cai, *Effect of Leading-Edge Protuberances Inspired by Humpback Whale Flipper on Airfoil Stall Control* (Tsinghua University, 2018).
- ²⁶K. Shanmukha Srinivas, A. Datta, A. Bhattacharyya, and S. Kumar, "Free-stream characteristics of bio-inspired marine rudders with different leading-edge configurations," *Ocean Eng.* **170**, 148–159 (2018).
- ²⁷R. Kant and A. Bhattacharyya, "A bio-inspired twin-protuberance hydrofoil design," *Ocean Eng.* **218**, 108209 (2020).
- ²⁸C. Cai, S. H. Liu, Z. G. Zuo, T. Maeda, Y. Kamada, Q. A. Li, and R. Sato, "Experimental and theoretical investigations on the effect of a single

- leading-edge protuberance on airfoil performance," *Phys. Fluids* **31**, 027103 (2019).
- ²⁹I. Celik, U. Ghia, P. J. Roache, and C. J. Freitas, "Procedure for estimation and reporting of uncertainty due to discretization in CFD applications," *J. Fluids Eng.* **130**, 078001 (2008).
- ³⁰B. C. Khoo, "Study on flow separation and transition of the airfoil in low Reynolds number," *Phys. Fluids* **31**, 103601 (2019).
- ³¹R. Wang and Z. Xiao, "Transition effects on flow characteristics around a static two-dimensional airfoil," *Phys. Fluids* **32**, 3 (2020).
- ³²R. B. Langtry and F. R. Menter, "Correlation-based transition modeling for unstructured parallelized computational fluid dynamics codes," *AIAA J.* **47**, 2894–2906 (2009).
- ³³R. B. Langtry, F. R. Menter, S. R. Likki, Y. B. Suzen, P. G. Huang, and S. Völker, "A correlation-based transition model using local variables—part II: Test cases and industrial applications," *J. Turbomach.* **128**, 423–434 (2006).
- ³⁴H. Chang, C. Cai, D. Y. Li, and Z. G. Zuo, "Effect of twin leading-edge protuberances on airfoil performance" AIAA J. (submitted).